A Fractional-order Image Segmentation Model With Application to Low-Contrast and Piecewise Smooth Images

Junfeng Cao[a*], Ke Chen[b], Huan Han[c]

a School of Science, Jiangnan University , Wuxi 214122, China

b Department of Mathematical Sciences, University of Liverpool, L69 3BX, United Kingdom

c Department of Mathematics, Wuhan University of Technology, Wuhan 430070, China

Abstract

In this paper, we propose a two-stage image segmentation model based on structure tensor and fractional-order regularization. In the first stage, we use the fractional-order regularization to approximate the Hausdorff measure of the Mumford-Shah (MS) model. The existence and uniqueness of the solution is proved and the alternating direction implicit (ADI) scheme is used to find the solution of the modified MS model. In the second stage, a thresholding is used to induce the segmentation of the target. The superior performances of the proposed model are demonstrated by some comparative experimental results with several state-of-art methods.

Keywords: fractional-order, image segmentation, structure tensor, ADI

1. Introduction

Image segmentation is an important topic in many scientific areas. It has been extensively studied and plays a significant role in many fields, such as atmospheric science, medical imaging, computer sicence, etc [1–6]. The main goal of image segmentation is to partition an image into several distinct constituents. During the past decades, numerous models and algrithms have been extensively proposed for image segmentation [7–11]. In the process of computing image segmentation models, the variational method has been widely applied to minimize the energy functionals [12–15].

In 1989, Mumford and Shah proposed a typical region-based model called Mumford-Shah model (MS model) [16], which was a landmark achievement in image segmentation fields. The MS model formulated as:

$$E_{MS}(u, \Gamma, \Omega) = \frac{\lambda}{2} \int_{\Omega} (f - u)^2 dx + \frac{\eta}{2} \int_{\Omega \backslash \Gamma} |\nabla u|^2 dx + Length(\Gamma), \qquad (1.1)$$

where $\Omega \subset R^2$ is a bounded open connected set and Γ is a compact curve in Ω, λ and η are positive parameters, $f : \Omega \to R$ is the degraded image and $u : \Omega \to R$ is the

---

*Corresponding author.

Email addresses: `caojunfeng982@163.com` (Junfeng Cao[a]), `k.chen@liv.ac.uk` (Ke Chen[b]), `hanhuan11@whut.edu.cn` (Huan Han[c])

optimal piecewise continuous or piecewise constant approximation of the given image f, $Length(\Gamma)$ represents the length of Γ which can be written as 1-dimensional Hausdorff measure $\mathscr{H}^1(\Gamma)$ in R^2.

Based on framework (1.1), many modified versions of MS model [17–19] have been proposed. Most of these works mainly focus on the simplification of MS model. For example, the Chan-Vese model (CV model)[20] which segmented the image into two parts(i.e., background and foreground) and modelled the solution to be a piecewise constant function. Furthermore, there are also some generalized versions of CV model, we refer the readers to [21–23] for details. These methods perform well for certain image segmentation tasks. However, they are easily trapped into local minimum because of its non-convexity. To address this dilemma, convex approximation approaches have been proposed. Recently, Cai et al. proposed a two-stage image segmentation strategy [24]. The strategy is divided the segmentation task into two steps. The first step is essentially a image restoration task, which aims to search for a smooth minimizer to estimate a clean image from the degraded image. For this purpose, the smooth minimizer g is obtained by solving the following variational problem:

$$\inf_{g} \frac{\lambda}{2} \int_{\Omega} (f - \mathscr{A}u)^2 dx + \frac{\eta}{2} \int_{\Omega} |\nabla u|^2 dx + \int_{\Omega} |\nabla u| dx \qquad (1.2)$$

where $\mathscr{A}$ is an identity operator or a blurring operator. The second step is image segmentation which is done by thresholding u properly. The two-stage strategy and corresponding improved model have remarkable virtues in image segmentation refer to [25–27] for details.

Essentially, the improvement for (1.1) comes from the substitution of $Length(\Gamma)$ with a convex total variation (TV) regularization $\int_{\Omega} |\nabla u| dx$. However, some applications [28–30] have indicated that the model with non-convex regularization can recover sharp and neat edges better. In order to achieve the better approximation for the Hausdorff measure and preserve the boundary information of the object better, Wu et al. proposed another two-stage strategy image segmentation based on nonconvex $l_1 - l_p$ approximation and thresholding [31], by replacing the first stage in [25] with the following smoothing process:

$$\inf_{u} \frac{\lambda}{2} \int_{\Omega} (f - \mathscr{A}u)^2 dx + \frac{\eta}{2} \int_{\Omega} |\nabla u|^2 dx + \int_{\Omega} |\nabla u|^p dx, \qquad (1.3)$$

where $0 < p < 1$.

Furthermore, in order to obtain the more accurate approximation for the Hausdorff measure and utilize the information of the image, many researchers proposed several schemes to substitute the regularization. Pang et.al introuced an adaptive weighted TV^p regularization-based image denoising model [32]. Wu et.al developed a novel adaptive total variation based image segmentation model [33]. The other researchers adopt the fractional-order deritive to formulate the image processing problem [34–36]. In [37], Zhang et al. introduced a fractional-order denoising model by replacing ∇u in total variation model with $\nabla^\alpha u$. Han [38] proposed a tensor voting based fractional-order image denoising model. In these models, $\nabla^\alpha u$ is the unique characteristic vector of image structure. Motivated by [38], we propose a tensor voting based fractional-order image segmentation

2

model. The nonconvex approximation of the MS model of our method can be expressed as the following:

$$\inf_u \frac{\lambda}{2} \int_\Omega (f - \mathscr{A}u)^2 dx + \frac{\eta}{2} \int_\Omega |\nabla u|^2 dx + \int_\Omega c(x)|\nabla^\alpha u|^2 dx, \tag{1.4}$$

where the first term in (1.4) is the fidelity, the second term is l_2 regularization and the third term is the tensor voting based fractional-order regularization. α is the fractioal order and value is between 1 and 2, $\nabla^\alpha u = \left(\frac{\partial^\alpha u}{\partial x_1^\alpha}, \frac{\partial^\alpha u}{\partial x_1^\alpha}\right)^T$. Moreover, here the tensor structure function $c(x)$ is defined by

$$c(x) = k + e^{-[|\mu_1 \mu_2| + |\mu_1 - \mu_2|^2]}, \qquad k > 0, \tag{1.5}$$

and $\mu_1(x), \mu_2(x)$ are the eigenvalues of the structure tensor (ST)

$$T(x) = G_\sigma * \begin{pmatrix} \left(\frac{\partial u}{\partial x_1}\right)^2 & \frac{\partial^2 u}{\partial x_1 \partial x_2} \\ \frac{\partial^2 u}{\partial x_1 \partial x_2} & \left(\frac{\partial u}{\partial x_2}\right)^2 \end{pmatrix} = \begin{pmatrix} u_{11}(x) & u_{12}(x) \\ u_{12}(x) & u_{22}(x) \end{pmatrix}, \tag{1.6}$$

here G_σ is Gaussian kernel.

As we all know, in the field of image processing, structure tensor is used to characterize the information such as textures, corner and edge of image [40, 41]. Therefore, we introduce a tensor voting function $c(x)$ in our model to deal with the various characteristics in different regions. Furthermore, $\nabla^\alpha u$ is the unique character vector of image structure. In our model, we combine these two factors. In flat region, $c(x) \to k + 1$, regulazation term plays a major role. While on edge or corner $c(x) \to k$, the fitting term begins to play a dominant role. Utilize some good properties of discretized fractional-order derivatives, we suppose that $\alpha \in (1, 2)$. To demonstrate the merits of the tensor voting based fractional-order regularization term, we simulate the regularization term of the image in Figure 1. $I(x)$ are two given original images which are shown in the first column of Figure 1. The structuer tensor and the fractional-order gradient of images are presented in the second and third columns in Figure 2. We can see that the edges are more prominent. This observations is the main motivation for us to add the term combined these two features into our model.

The organization of the paper is as follows: in Section 1, some background on image segmentation model is reviewed, and our tensor voting based fractional-order image segmentation model is introduced. In Section 2, the existence and uniqueness of solution of model (1.4) is proved. In Section 3, an alternating direction implicit (ADI) scheme of model (1.4) is proposed. Numerical experiments are list in Section 4, which clearly exhibit the performance of the proposed approach. Finally, the conclusions are summarized in Section 5.

At the end of this section, we list the following notations and definitions used in this paper:

- For $x = (x_1, x_2) \in \Omega = (a_1, b_1) \times (a_2, b_2)$ and function $f : \Omega \to \mathbb{R}$, define

$$\frac{\partial^\alpha f(x)}{\partial x_i^\alpha} \triangleq \frac{1}{\Gamma([\alpha] + 1 - \alpha)} \left(\frac{d}{dx_i}\right)^{[\alpha]+1} \int_{a_i}^{x_i} \frac{f^{(i)}(x, t)}{(x_i - t)^{\alpha - [\alpha]}} dt, \tag{1.7}$$

3

Fig. 1: Structure tensor and fractional-order gradient of the images.

$$\frac{\partial^{\alpha*} f(x)}{\partial x_i^{\alpha*}} \triangleq \frac{1}{\Gamma([\alpha]+1-\alpha)} \left(-\frac{d}{dx_i}\right)^{[\alpha]+1} \int_{x_i}^{b_i} \frac{f^{(i)}(x,t)}{(t-x_i)^{\alpha-[\alpha]}} dt, \qquad (1.8)$$

where here and in what follows, $\Gamma(s) = \int_0^{+\infty} x^{s-1} e^{-x} dx$, $[\cdot]$ is round down function, $f^{(1)}(x,t) = f(t,x_2)$, $f^{(2)}(x,t) = f(x_1,t)$ and $i = 1,2$.

- Division of Ω: we define a spatial partition $P_{i,j} = (x_i, y_j) = (a_1 + ih_1, b_1 + jh_2)$(for all $i = 0, 1, \cdots, N_1+1; j = 0, 1, \cdots, N_2+1$) of image Ω and a time partition $s_k = k\gamma$(for all $k = 0, 1, 2, \cdots, N$) of interval $[0, \tau]$, where $\gamma = \tau/N$, $h_1 = (a_2 - a_1)/(N_1 + 1)$, $h_2 = (b_2 - b_1)/(N_2 + 1)$.

- $\rho_0^{(\alpha)} = 1$, $\rho_j^{(\alpha)} = \left(1 - \frac{1+\alpha}{j}\right)\rho_{j-1}^{(\alpha)}$.

- $\delta_{1-}^\alpha f_{i,j} = \frac{1}{h_1^\alpha} \sum_{l=1}^{i+1} \rho_l^{(\alpha)} f_{i-l+1,j}$, $\delta_{1+}^\alpha f_{i,j} = \frac{1}{h_1^\alpha} \sum_{l=1}^{N_1-i+2} \rho_l^{(\alpha)} f_{i+l-1,j}$.

- $\delta_{2-}^\alpha f_{i,j} = \frac{1}{h_2^\alpha} \sum_{m=1}^{j+1} \rho_m^{(\alpha)} f_{i,j-m+1}$, $\delta_{2+}^\alpha f_{i,j} = \frac{1}{h_2^\alpha} \sum_{m=1}^{N_2-j+2} \rho_m^{(\alpha)} f_{i,j+m-1}$.

2. Existence and uniqueness of solution of model (1.4)

Then we prove the existence and uniqueness of solution of model (1.4). As to this problem, we have the following result:

Theorem 2.1. *Assume $0 < c_0 \le c(x) \le c_1 < +\infty$ for all $x \in \Omega$, $\mathscr{A}$ is a linear bound operator, then (1.4) admits a unique solution $u \in H_0^\alpha(\Omega)$.*

Proof. Select a minimizing sequence $\{u^k\} \in H_0^\alpha(\Omega)$, then

$$c_0 \int_\Omega |\nabla^\alpha u^k|^2 dx \le E(u^k) = \frac{\lambda}{2} \int_\Omega (\mathscr{A} u^k - f)^2 dx + \frac{\eta}{2} \int_\Omega |\nabla u^k|^2 dx + \int_\Omega c(x)|\nabla^\alpha u^k|^2 dx < +\infty.$$
$$(2.1)$$

4

That is, $\{u^k\}$ is bounded on $BV_2^\alpha(\Omega)$. By [35], there exists a $u \in BV_2^\alpha(\Omega)$ and a subsequence $\{u^k\}$ which is still labeled by u^k such that $\|u^k - u\|_{L^2(\Omega)} \to 0$ and

$$\int_\Omega \nabla^\alpha u^k \cdot w dx \to \int_\Omega \nabla^\alpha u \cdot w dx \quad \forall w \in C_0^\infty(\Omega). \tag{2.2}$$

$$\int_\Omega \nabla u^k \cdot v dx \to \int_\Omega \nabla u \cdot v dx \quad \forall v \in C_0^\infty(\Omega). \tag{2.3}$$

Let $w = c\nabla^\alpha u$ and $v = \nabla u$ in (2.2) and (2.3), then there holds,

$$\int_\Omega c|\nabla^\alpha u|^2 dx = \lim_{k \to +\infty} \int_\Omega c\nabla^\alpha u^k \cdot \nabla^\alpha u dx \leq \lim_{k \to +\infty} \left(\int_\Omega c|\nabla^\alpha u^k|^2 dx \right)^{\frac{1}{2}} \left(\int_\Omega c|\nabla^\alpha u|^2 dx \right)^{\frac{1}{2}}, \tag{2.4}$$

and

$$\int_\Omega |\nabla u|^2 dx = \lim_{k \to +\infty} \int_\Omega \nabla u^k \cdot \nabla u dx \leq \lim_{k \to +\infty} \left(\int_\Omega |\nabla u^k|^2 dx \right)^{\frac{1}{2}} \left(\int_\Omega |\nabla u|^2 dx \right)^{\frac{1}{2}}. \tag{2.5}$$

Therefore, we have that

$$\int_\Omega c|\nabla^\alpha u|^2 dx \leq \liminf_{k \to +\infty} \int_\Omega c|\nabla^\alpha u^k|^2 dx, \tag{2.6}$$

and

$$\int_\Omega |\nabla u|^2 dx \leq \liminf_{k \to +\infty} \int_\Omega |\nabla u^k|^2 dx. \tag{2.7}$$

On the other hand, by the fact $\|u^k - u\|_{L^2(\Omega)} \to 0$ and $\mathscr{A}$ is a linear bound operator, we conclude $\|\mathscr{A}u^k - \mathscr{A}u\|_{L^2(\Omega)} \to 0$ because of the fact that

$$\left| \int_\Omega (\mathscr{A}u - f)^2 dx - \int_\Omega (\mathscr{A}u^k - f)^2 dx \right|$$
$$= \left| \int_\Omega (\mathscr{A}u^k - \mathscr{A}u)(\mathscr{A}u^k + \mathscr{A}u - 2f) dx \right|$$
$$\leq \|\mathscr{A}u^k - \mathscr{A}u\|_{L^2(\Omega)} \left(\|\mathscr{A}u^k - f\|_{L^2(\Omega)} + \|\mathscr{A}u - f\|_{L^2(\Omega)} \right) \to 0. \tag{2.8}$$

Note that here we use the fact $\|\mathscr{A}u^k - f\|_{L^2(\Omega)}$, $\|\mathscr{A}u - f\|_{L^2(\Omega)}$ are bounded and $\|\mathscr{A}u^k - \mathscr{A}u\|_{L^2(\Omega)} \leq \|\mathscr{A}\|\|u^k - u\|_{L^2(\Omega)}$.

By (2.6), (2.7) and (2.8), we know that

$$E(u) \leq \liminf_{k \to +\infty} E(u^k). \tag{2.9}$$

This implies, there exists a $u \in H^\alpha(\Omega)$ such that $u = \arg \min_{u \in H_0^\alpha(\Omega)} E(u)$.

Uniqueness of solution follows from the strict convexity of $E(u)$.

5

3. Numerical algorithm for Fractional-order Image Segmentation Model

3.1. ADI scheme of the image segmentation model

In this section, we mainly focus on the numerical implementation of model (1.4). First, we calculate Euler-Lagrange equation of problem (1.4):

Theorem 3.1. *The Euler-Lagrange equation of (1.4) can be written as*

$$\text{div}^{\alpha*}\left(c\nabla^{\alpha}u\right) + \eta\text{div}\left(\nabla u\right) + \lambda\mathscr{A}^*\left(\mathscr{A}u - f\right) = 0. \tag{3.1}$$

Proof. Assume $u \in H_0^{\alpha}(\Omega)$ is perturbed along $w \in H_0^{\alpha}(\Omega)$, then

$$\partial_w E(u) = 2\int_{\Omega} \text{div}^{\alpha*}\left(c\nabla^{\alpha}u\right) + \eta\text{div}\left(\nabla u\right) + \lambda\mathscr{A}^*\left(\mathscr{A}u - f\right)] \cdot wdx. \tag{3.2}$$

Note that here $u, w \in F_{L,0}^{\alpha}(\Omega) = H_0^{\alpha}(\Omega)$[34–36] implies, $\frac{\partial^k g(x)}{\partial x_i^k}|_{x\in\partial\Omega} = 0$, $(k = 0, 1, 2, \cdots, [\alpha]; i = 1, 2, 3)$(cf. Sobolev space in [34, 35]). That is, any function on $F_{L,0}^{\alpha}(\Omega)$ satisfies the homogeneous boundary conditions. This implies two important properties of fractional derivatives we used to derive (3.2):

(i). In this sense, Riemann-Liouville derivatives, Grunwald-Letnikov derivatives and Caputo derivatives are equivalent [37].

(ii). Integration by parts formula

$$\int_{a_i}^{b_i} \xi(x) \cdot \frac{\partial^{\alpha} f(x)}{\partial x_i^{\alpha}}dx_i = \int_{a_i}^{b_i} \frac{\partial^{\alpha*}\xi(x)}{\partial x_i^{\alpha*}} \cdot f(x)dx_i \quad i = 1, 2, 3. \tag{3.3}$$

It follows from the variational principle and (3.2) that

$$\text{div}^{\alpha*}\left(c\nabla^{\alpha}u\right) + \eta\text{div}\left(\nabla u\right) + \lambda\mathscr{A}^*\left(\mathscr{A}u - f\right) = 0. \tag{3.4}$$

$$\square$$

To solve (3.1), we use the gradient flow to update u to the steady state of following fractional-order evolution equations:

$$\frac{1}{2}\frac{\partial u}{\partial s} + \text{div}^{\alpha*}\left(c\nabla^{\alpha}u\right) + \eta\text{div}\left(\nabla u\right) + \lambda\mathscr{A}^*\left(\mathscr{A}u - f\right) = 0. \tag{3.5}$$

For the purpose of solving (3.5) approximately, $\frac{\partial^{\alpha}u(x)}{\partial x_k^{\alpha}}$, $\frac{\partial^{\alpha*}u(x)}{\partial x_k^{\alpha*}}(k = 1, 2)$ are approximated by(cf. [37, 42]):

$$\frac{\partial^{\alpha}u(P_{i,j})}{\partial x_k^{\alpha}} = \delta_{k-}^{\alpha}u(P_{i,j}) + O(h_k), \quad \frac{\partial^{\alpha*}u(P_{i,j})}{\partial x_k^{\alpha*}} = \delta_{k+}^{\alpha}u(P_{i,j}) + O(h_k). \tag{3.6}$$

Furthermore, when $\alpha = 1$, we can obtain $\nabla^{\alpha}u = \nabla u$.To overcome the large computational cost and keep the stability of scheme, we use the alternative direction implicit(ADI) scheme [35, 43] to solve (3.5).

6

This equation can be written as

$$\frac{1}{2}\frac{\partial u^{n+1}}{\partial s} + \frac{1}{2}\text{div}^{\alpha*}\left(c\nabla^{\alpha}u^{n+1}\right) + \frac{1}{2}\text{div}^{\alpha*}\left(c\nabla^{\alpha}u^{n}\right)$$
$$+\frac{\eta}{2}\text{div}\left(\nabla u^{n+1}\right) + \frac{\eta}{2}\text{div}\left(\nabla u^{n}\right) + \lambda\mathscr{A}^{*}\mathscr{A}u^{n+1} - \lambda\mathscr{A}^{*}f = 0. \tag{3.7}$$

Suppose $\mathscr{A}$ is a positive definite matrix whose singular value decomposition is $\mathscr{A} = USV^{T}$, where U, V are two orthogonal matrices. Therefore, we have that $\mathscr{A}^{T}\mathscr{A} = (USV^{T})^{T}USV^{T} = VSU^{T}USV^{T} = VSV^{T} = VSV^{T}VSV^{T} = (VSV^{T})^{2}$. Let $M = VSV^{T}$, then we conclude that $\mathscr{A}^{T}\mathscr{A} = M^{2}$ That is,

$$\frac{u_{i,j}^{n+1} - u_{i,j}^{n}}{2\gamma} + \frac{1}{2}\left[\delta_{1+}^{\alpha}(c_{i,j}\delta_{1-}^{\alpha}) + \eta\delta_{1+}(\delta_{1-}) + \delta_{2+}^{\alpha}(c_{i,j}\delta_{2-}^{\alpha}) + \eta\delta_{2+}(\delta_{2-})\right](u_{i,j}^{n+1} + u_{i,j}^{n})$$
$$+\lambda(M_{i,j})^{2}u_{i,j}^{n+1} - \lambda(\mathscr{A}^{T}f)_{i,j} = 0 \tag{3.8}$$

Adding some higher order terms on the left side of (3.8), yields

$$\frac{\gamma}{2}\left[\frac{1}{\gamma} + \sqrt{\lambda}M_{i,j} + \delta_{1+}^{\alpha}(c_{i,j}\delta_{1-}^{\alpha}) + \eta\delta_{1+}(\delta_{1-})\right]\left[\frac{1}{\gamma} + \sqrt{\lambda}M_{i,j} + \delta_{2+}^{\alpha}(c_{i,j}\delta_{2-}^{\alpha}) + \eta\delta_{2+}(\delta_{2-})\right]u_{i,j}^{n+1} =$$
$$\frac{\gamma}{2}\left[\frac{1}{\gamma} - \delta_{1+}^{\alpha}(c_{i,j}\delta_{1-}^{\alpha}) - \eta\delta_{1+}(\delta_{1-})\right]\left[\frac{1}{\gamma} - \delta_{2+}^{\alpha}(c_{i,j}\delta_{2-}^{\alpha}) - \eta\delta_{2+}(\delta_{2-})\right]u_{i,j}^{n} + \lambda(\mathscr{A}^{T}f)_{i,j}. \tag{3.9}$$

Therefore, we obtain the following ADI scheme of model (1.4):

$$\begin{cases} \frac{\gamma}{2}\left[\frac{1}{\gamma} + \sqrt{\lambda}M_{i,j} + \delta_{1+}^{\alpha}(c_{i,j}\delta_{1-}^{\alpha}) + \eta\delta_{1+}(\delta_{1-})\right]u_{i,j}^{n+\frac{1}{2}} = F_{i,j}^{n}, \\ \left[\frac{1}{\gamma} + \sqrt{\lambda}M_{i,j} + \delta_{2+}^{\alpha}(c_{i,j}\delta_{2-}^{\alpha}) + \eta\delta_{2+}(\delta_{2-})\right]u_{i,j}^{n+1} = u_{i,j}^{n+\frac{1}{2}}, \end{cases} \tag{3.10}$$

where $F_{i,j}^{n} = \frac{\gamma}{2}\left[\frac{1}{\gamma} - \delta_{1+}^{\alpha}(c_{i,j}\delta_{1-}^{\alpha}) - \eta\delta_{1+}(\delta_{1-})\right]\left[\frac{1}{\gamma} - \delta_{2+}^{\alpha}(c_{i,j}\delta_{2-}^{\alpha}) - \eta\delta_{2+}(\delta_{2-})\right]u_{i,j}^{n} + \lambda(\mathscr{A}^{T}f)_{i,j}$.

(3.10) can be reformulated into the following matrix form:

$$\begin{cases} \frac{\gamma}{2}\left[\left(\frac{1}{\gamma} + \sqrt{\lambda}M_{i,j}\right)I_{N_1} + B_j\right]V_j^{n+\frac{1}{2}} = H_j^n, \\ \left[\left(\frac{1}{\gamma} + \sqrt{\lambda}M_{i,j}\right)I_{N_2} + A_i\right]U_i^{n+1} = G_i^{n+\frac{1}{2}}, \end{cases} \tag{3.11}$$

where $V_j^{n+\frac{1}{2}} = (u_{1,j}^{n+\frac{1}{2}}, u_{2,j}^{n+\frac{1}{2}}, \cdots, u_{N_1,j}^{n+\frac{1}{2}})^T$, $U_i^{n+1} = (u_{i,1}^{n+1}, u_{i,2}^{n+1}, \cdots, u_{i,N_2}^{n+1})^T$, $H_j^n = (F_{1,j}^n, F_{2,j}^n, \cdots, F_{N_1,j}^n)^T$, $G_i^{n+\frac{1}{2}} = (u_{i,1}^{n+\frac{1}{2}}, u_{i,2}^{n+\frac{1}{2}}, \cdots, u_{i,N_2}^{n+\frac{1}{2}})^T$, $B_j = C_j^T C_j$, $A_i = D_i^T D_i$, $C_j = \Lambda_j L_{N_1}$, $D_i = \bar{\Lambda}_i L_{N_2}$, $I_S(S = N_1, N_2)$ denotes the unit matrix of order S, $\Lambda_j = diag(\sqrt{c_{1,j}}, \sqrt{c_{2,j}} \cdots \sqrt{c_{N_1,j}})$, $\bar{\Lambda}_i = diag(\sqrt{c_{i,1}}, \sqrt{c_{i,2}} \cdots \sqrt{c_{i,N_2}})$,

$$L_{N_1} = \frac{1}{h_1^\alpha}\begin{pmatrix} \rho_1^{(\alpha)} & \rho_0^{(\alpha)} & 0 & \cdots & 0 \\ \rho_2^{(\alpha)} & \rho_1^{(\alpha)} & \rho_0^{(\alpha)} & \cdots & 0 \\ \vdots & \vdots & \ddots & \cdots & \vdots \\ \rho_{N_1-1}^{(\alpha)} & \rho_{N_1-2}^{(\alpha)} & \cdots & \rho_1^{(\alpha)} & \rho_0^{(\alpha)} \\ \rho_{N_1}^{(\alpha)} & \rho_{N_1-1}^{(\alpha)} & \cdots & \rho_2^{(\alpha)} & \rho_1^{(\alpha)} \end{pmatrix} + \frac{\eta}{h_1}\begin{pmatrix} \rho_1 & \rho_0 & 0 & \cdots & 0 \\ \rho_2 & \rho_1 & \rho_0 & \cdots & 0 \\ \vdots & \vdots & \ddots & \cdots & \vdots \\ \rho_{N_1-1} & \rho_{N_1-2} & \cdots & \rho_1 & \rho_0 \\ \rho_{N_1} & \rho_{N_1-1} & \cdots & \rho_2 & \rho_1 \end{pmatrix},$$

7

$$L_{N_2} = \frac{1}{h_2^\alpha} \begin{pmatrix} \rho_1^{(\alpha)} & \rho_0^{(\alpha)} & 0 & \cdots & 0 \\ \rho_2^{(\alpha)} & \rho_1^{(\alpha)} & \rho_0^{(\alpha)} & \cdots & 0 \\ \vdots & \vdots & \ddots & \cdots & \vdots \\ \rho_{N_2-1}^{(\alpha)} & \rho_{N_2-2}^{(\alpha)} & \cdots & \rho_1^{(\alpha)} & \rho_0^{(\alpha)} \\ \rho_{N_2}^{(\alpha)} & \rho_{N_2-1}^{(\alpha)} & \cdots & \rho_2^{(\alpha)} & \rho_1^{(\alpha)} \end{pmatrix} + \frac{\eta}{h_2^\alpha} \begin{pmatrix} \rho_1 & \rho_0 & 0 & \cdots & 0 \\ \rho_2 & \rho_1 & \rho_0 & \cdots & 0 \\ \vdots & \vdots & \ddots & \cdots & \vdots \\ \rho_{N_2-1} & \rho_{N_2-2} & \cdots & \rho_1 & \rho_0 \\ \rho_{N_2} & \rho_{N_2-1} & \cdots & \rho_2 & \rho_1 \end{pmatrix}.$$

Remark 3.1. *In algorithm of [37], it is expected to compute the inverse of a $N_1 \times N_2$ order matrix. However, this costs too much computer memory and time. ADI scheme (3.11) divides 2D problem into several 1D problems. This scheme not only keeps the stability of algorithm and saves much computer memory(cf. [36]), but also can be extended to 3D image segmentation problems. In 3D case, the advantage of this scheme can be even more obvious. This is the main motivation for us to design the numerical scheme (3.11).*

3.2. Thresholding

In this stage, the segmentation results can be obtained by separating the u which is the smooth approximation in the first stage. We should to calculate the threshold values to segment u into K parts. Here, we use the K-means clustering method. We firstly normalize the smooth image u. The pixel values of u are restricted to $\tilde{u} \in [0, 1]$. Suppose $\sum_1 \cup \sum_2 \cup \cdots \cup \sum_K = \Omega$. The cluster center $\tilde{\rho}_k$ can be calculated by

$$\tilde{\rho}_k = \frac{\int_{\sum_k} u \mathrm{d}x}{\int_{\sum_k} \mathrm{d}x} \qquad (k = 1, 2, \cdots, K) \tag{3.12}$$

Without loss of generality, let $\tilde{\rho}_1 \leq \tilde{\rho}_2 \leq \cdots \leq \tilde{\rho}_K$. Then, the thresholds are given by:

$$\rho_i = \frac{\tilde{\rho}_i + \tilde{\rho}_{i+1}}{2} \qquad (i = 1, 2, \cdots, K-1) \tag{3.13}$$

Using the thresholding value, we can obtained the *kth* segments of $\tilde{u}$ by

$$\Omega_k = \{x \in \Omega : \rho_{i-1} \leq \tilde{u}(x) \leq \rho_i\} \qquad (k = 1, 2, \cdots, K) \tag{3.14}$$

Based on these notations, the ADI scheme of the tensor voting based fractional-order image segmentation algorithm can be summarized as follows Algorithm 1.

4. Numerical Experiments

In this section, we conduct numerical experiments to show the efficiency of the tensor voting based fractional-order image segmentation algorithm proposed in Section 3. The numerical tests are performed using MATLAB (R2021a) with Windows 10 (64bit) and Intel Core i7-8550U CPU @ 1.80 GHz and 8G of RAM.

8

Algorithm 1 Tensor based fractional-order image segmentation algorithm based on ADI scheme (3.7)

Input: a_1, a_2, b_1, b_2, τ, N_1, N_2, N.

Stage 1:

Initiallization: Given initial values $u_{i,j}^0 = f_{i,j}$.

    for $n = 1:N$ **do**

    (1) Let u_{ij}^n be known data at time $t = t_n$. Solving linear systems (3.11) to obtain $u_{i,j}^{n+1}$ for $i = 1, 2, \cdots, N_1$, $j = 1, 2, \cdots, N_2$.

    (2) Check the stop condition. If satisfied, stop and update the smoothing approximation image to u^{n+1}, else set $n = n + 1$ and return to (1).

    return $u_{i,j}^N$ for $i = 0, 1, \cdots, N_1$, $j = 0, 1, \cdots, N_2$ and we obtain the final smoothing approximation image result u^N.

  Stage 2:

Choose K, use the K-means method to get ρ_i and the segments $\Omega_i, (i = 1, 2, \cdots, k)$ using (3.13) and (3.14).

Output: Phases $\Omega_i, (i = 1, 2, \cdots, k)$

4.1. Parameters Setting

In the proposed image segmentation Algorithm 1, there are three important parameters: α, λ and η. In oder to choose the optimal value of these parameters, we use some quantitative indicators such as Segmentation Accuracy (SA), Precision, Recall, F1-Score (F1), Kappa coefficient (κ) and Jaccard Similarity (JS). These indicators can be calculated by the stand confusion matrix which are exhibited in Table.1. The test images are choosed from the Weizamann segmentation dataset. These indicators are defined as the following:

1. Segmentation Accuracy (SA):

$$SA = \frac{TP + TN}{TP + TN + FP + FN} \tag{4.1}$$

2. Precision:

$$P = \frac{TP}{TP + FP} \tag{4.2}$$

3. Recall:

$$R = \frac{TP}{TP + FN} \tag{4.3}$$

4. F1-Score (F1)

$$F1 = \frac{2PR}{P + R} \tag{4.4}$$

where P and R represent Precision and Recall, respectively.

5. Kappa coefficient (κ)

$$\kappa = \frac{SA - P_e}{1 - P_e}, \quad with \quad P_e = \frac{(TP + FN)(TP + FP) + (FP + TN)(FN + TN)}{(TP + TN + FP + FN)^2} \tag{4.5}$$
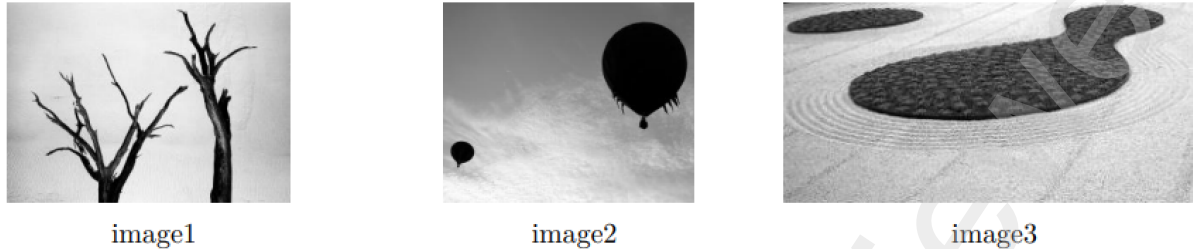
9

<div align="center">image1   image2   image3</div>

Fig. 2: Test images: Choose from the Weizmann dataset. Image1: Tree; Image 2: balloon; Image 3: Partorre.

Confusion matrix		True	
		Positive	Negative
Predict	Positive	TP	FP
	Negative	FN	TN

<div align="center">Table 1: Confusion matrix</div>

6. Jaccard Similarity (JS)

$$JS(S_1, S_2) = \frac{|S_1 \cap S_2|}{|S_1 \cup S_2|} \tag{4.6}$$

where S_1 is the region segmentated by the proposed algorithm and S_2 is the corresponding region in the ground truth. $|\cdot|$ repersents the number of pixels in image area.

As mentioned in section 2, we suppose $\alpha \in (1,2)$, we test the value of α from 1.2 to 1.9. The results of the six indicators which are estimated by our algorithm are exhibited in Figure 3. It is obviously that when $\alpha = 1.6$, the test images can obtain the best segmentation results.

In order to test the values of λ and η, we choose a cleaning image which is shown in Figure 4(a). We use the Matlab codes to create blur operator: "fspecial('motion', 50, 30)" and "fspecial('disk', 20)". The blur images are shown in Figure 4(b) and 4(c). We test the value of λ from 10 to 150. Some results are shown in Figure 4(d)-(i). Figure 4(j) is the ground truth. We can observed that when $\lambda \geq 60$ our method can chieve the best results. So we choose the λ from the interval $[80, 120]$ empirically. In the following tests, we only show the segmentation results with $\lambda = 100$. Then we test the parameter η from 1 to 10. From the results, we can see the contours of objects are almost unchanging. It indicates that our method is robust with the the parameter η. In the following tests, we choose $\eta = 1$.

When use the blur operator "fspecial('motion', 60, 45)", the parameters are set as: $\alpha = 2.4$, $\lambda = 200$ and $\eta = 1$, we can also obtain the right segmentation results. It proves that our method can still work when $\alpha > 2$.

4.2. Numerical segmentations

4.2.1. Image segmentation with different level of noise

In this expriment, we test our method on the artificial image with different noise level. As shown in Figure 5(a), 5(b) and 5(c), the image is added the Gaussian noises with mean 0 and variances 0.01, 0.015 and 0.02, respectively. Figure 5(d) and 5(e) are two synthetic
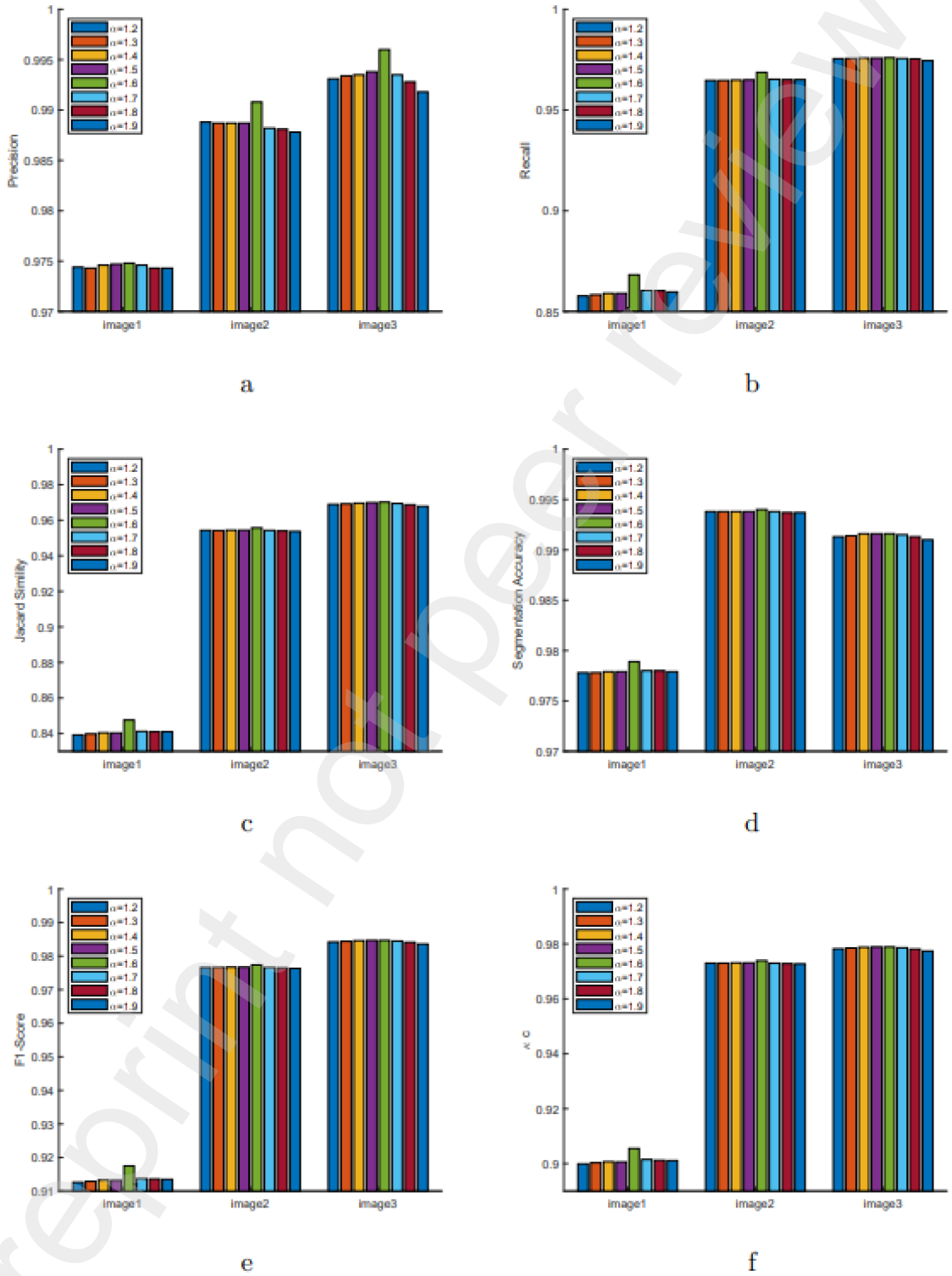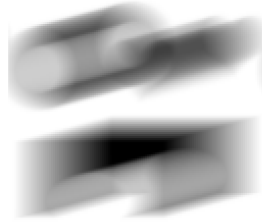
<div align="center">10</div>

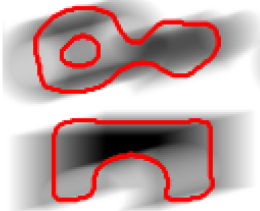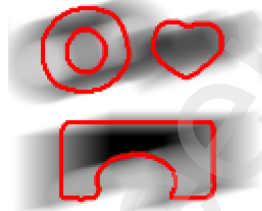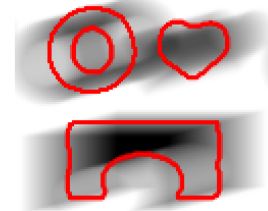**Fig. 3:** Six indecators of different values of α on test images.
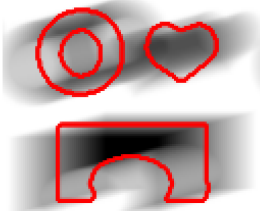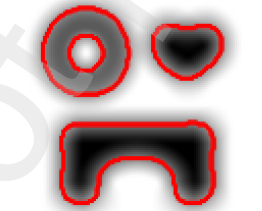
11

(a)Orignal image

(b)motion

(c)disk
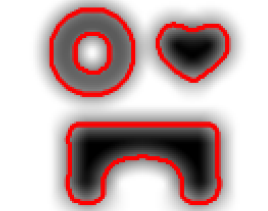
(d)$\lambda = 20; \mu = 1$
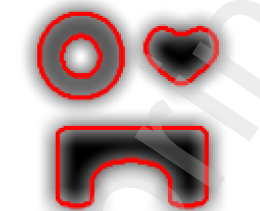
(e)$\lambda = 60; \mu = 1$

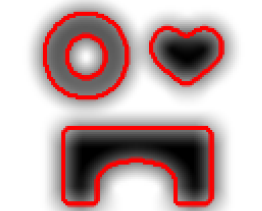(f)$\lambda = 100; \mu = 1$

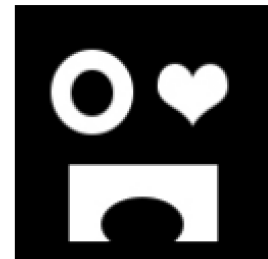(g)$\lambda = 150; \mu = 1$

(f)$\lambda = 20; \mu = 1$

(g)$\lambda = 60; \mu = 1$

(h)$\lambda = 100; \mu = 1$

(i)$\lambda = 150; \mu = 1$

(j)Ground truth

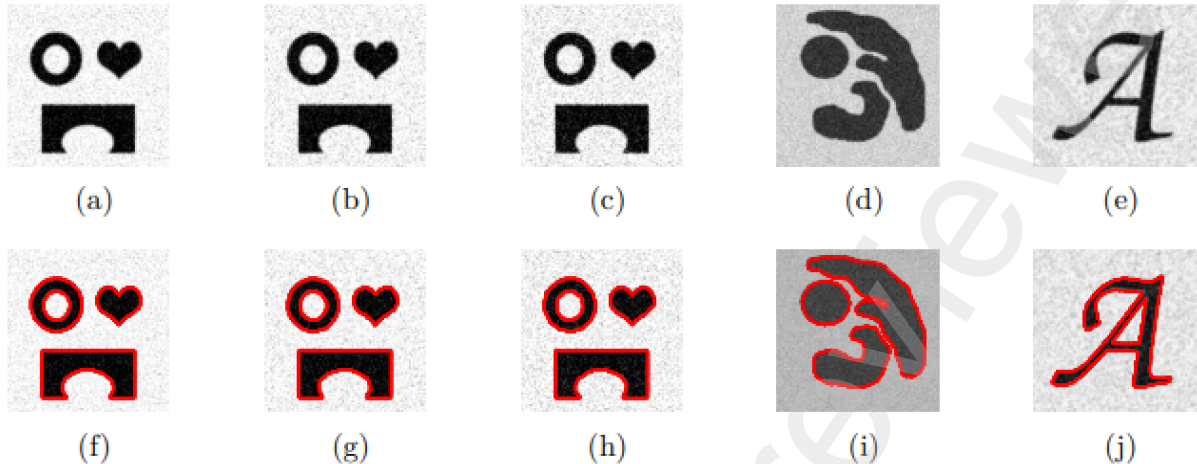**Fig.** 4: Segmentation results of two blur operators with different values of λ and η.

12

Fig. 5: Segmentation results of noisy images.

Algorithm	Js	F1	Recall	Precision	SA	κ
CV	0.8421	0.9143	0.8621	0.9733	0.9781	0.9081
LBF	0.3402	0.4144	0.4852	0.5164	0.4488	0.7759
SPGCS	0.9123	0.9029	0.8643	0.9723	0.9778	0.9049
LGDF	0.6573	0.7076	0.8213	0.8636	0.8510	0.8569
CCS	0.8315	0.9080	0.8582	0.9764	0.9726	0.8945
NAT	0.8441	0.9155	0.8643	0.9784	0.9784	0.9031
OUR	0.8476	0.9175	0.8682	0.9748	0.9789	0.9055

Table 2: Six indecators of the segmentation results shown in Figure 13.

images with noise. All the segmentation resuts are exbibited in figure 5(f) to 5(j). We can see that our model segments all the objects very well which indicates that our method is stable and robust with respect to the noise.

4.2.2. Image segmentation with weak boundaries

To futher comfirm the robustness and superiority of our method, we test our method on four images with different modalities. Figure 6(a) is a artificial synthetic image with the object like the letter "U". We can found that there is weak boundary in the lower left conner of "U". Figure 6(e), 6(i) and 6(m) are a militray infrared image, a medical image and a biomedical image respectively. All these images are intensity inhomogeneity, weak boundaries and low contract. The images in second column of Figure 6 are the restoration images. The segmentation results and the contours are demonstrsted in the third and fourth columns of figure 6. Our proposed model performs the satifatory segmentation results of all the images.

4.3. Comparison Experiments
4.3.1. Comparison with methed of [24] and method of [31]

In this experiment, we compare the proposed model with two classical two-stage segmentation algorithms proposed by [24] and [31]. We denote them as CCS and NAT.
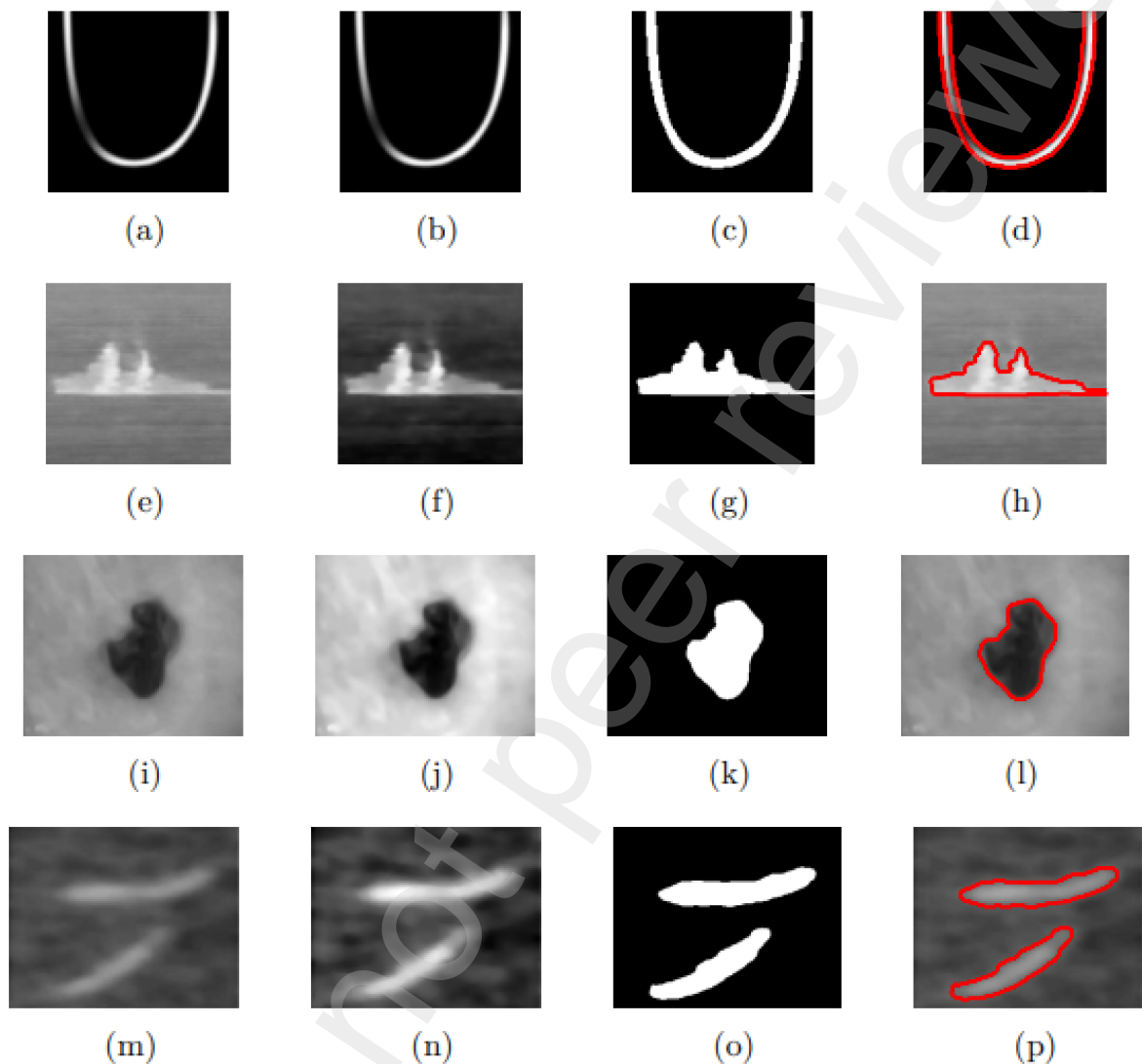
13

(a)   (b)   (c)   (d)

(e)   (f)   (g)   (h)

(i)   (j)   (k)   (l)

(m)   (n)   (o)   (p)

Fig. 6: Segmentation results of images with weak boundary and low constract.

Algorithm	Js	F1	Recall	Precision	SA	κ
CV	0.3402	0.3781	0.2107	0.4041	0.1683	0.7045
LBF	0.4888	0.4687	0.5479	0.5764	0.4983	0.7759
SPGCS	0.3060	0.3158	0.2643	0.3723	0.1778	0.7049
LGDF	0.9551	0.9771	0.9663	0.9881	0.9939	0.9735
CCS	0.9498	0.9742	0.9640	0.9931	0.9931	0.9703
NAT	0.9510	0.9749	0.9625	0.9933	0.9784	0.9710
OUR	0.9557	0.9774	0.9687	0.9948	0.9940	0.9739

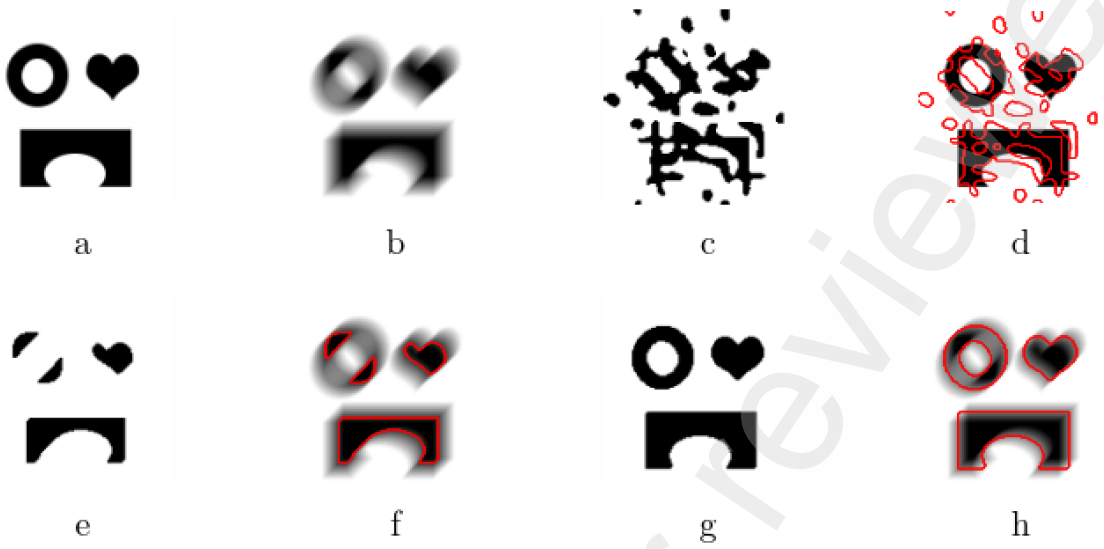Table 3: Six indecators of the segmentation results shown in Figure 14.

14

Fig. 7: The comparison between CCS, NAT and the proposed method on blur opertor "fspecial('motion', 20, 45)".
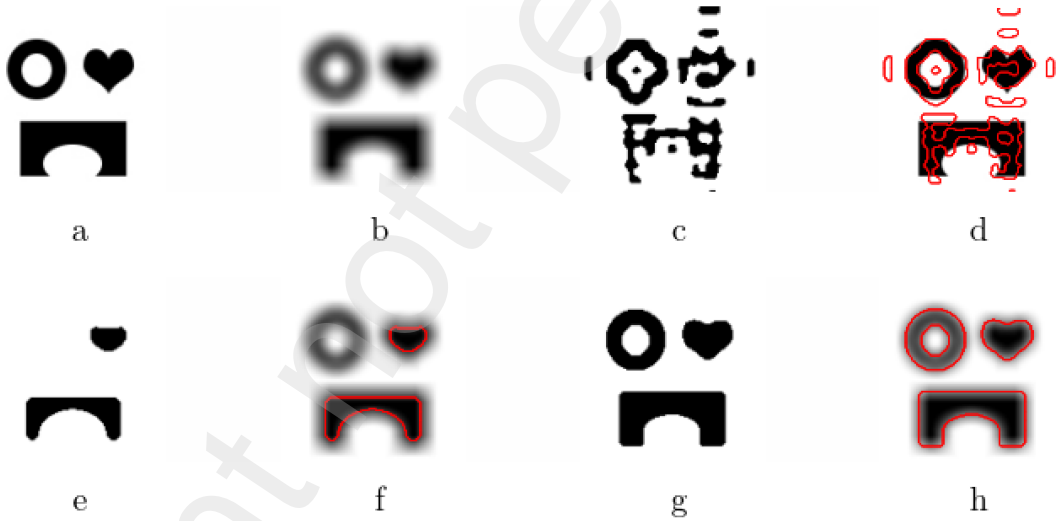

Fig. 8: The comparison between CCS, NAT and the proposed method on blur opertor "fspecial('Gaussian', [15,15], 15)".

Algorithm	Js	F1	Recall	Precision	SA	κ
CV	0.9231	0.9051	0.9313	0.9246	0.9912	0.9629
LBF	0.3712	0.4372	0.4687	0.6209	0.6414	0.6525
SPGCS	0.9073	0.9104	0.8936	0.9198	0.9526	0.8786
LGDF	0.6804	0.6781	0.6041	0.6447	0.6850	0.6525
CCS	0.9709	0.9852	0.9746	0.9919	0.9919	0.9797
NAT	0.9676	0.9835	0.9732	0.9910	0.9910	0.9773
OUR	0.9702	0.9847	0.9760	0.9960	0.9916	0.9789

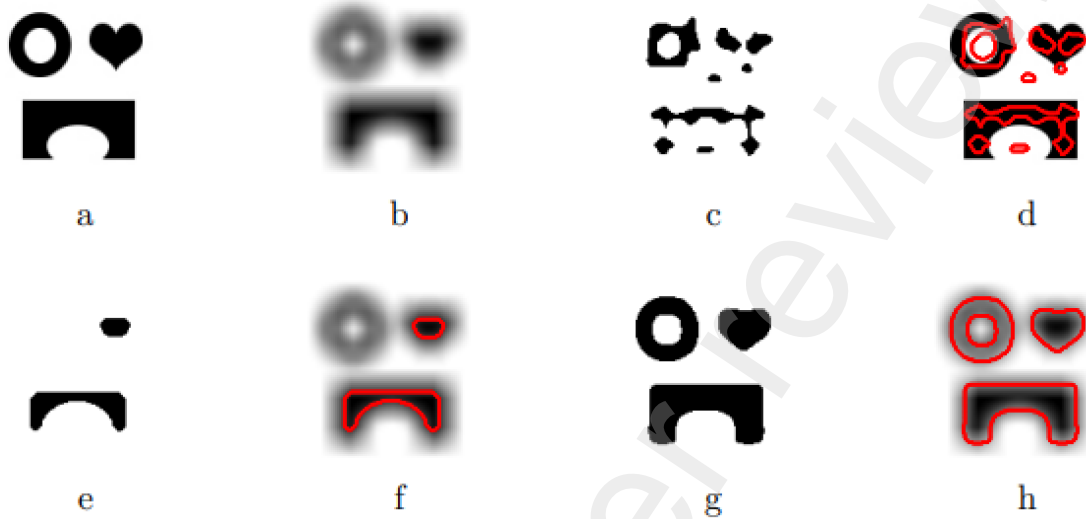Table 4: Six indecators of the segmentation results shown in Figure 15.

15

Fig. 9: The comparison between CCS, NAT and the proposed method on blur opertor "fspecial('average',20)".
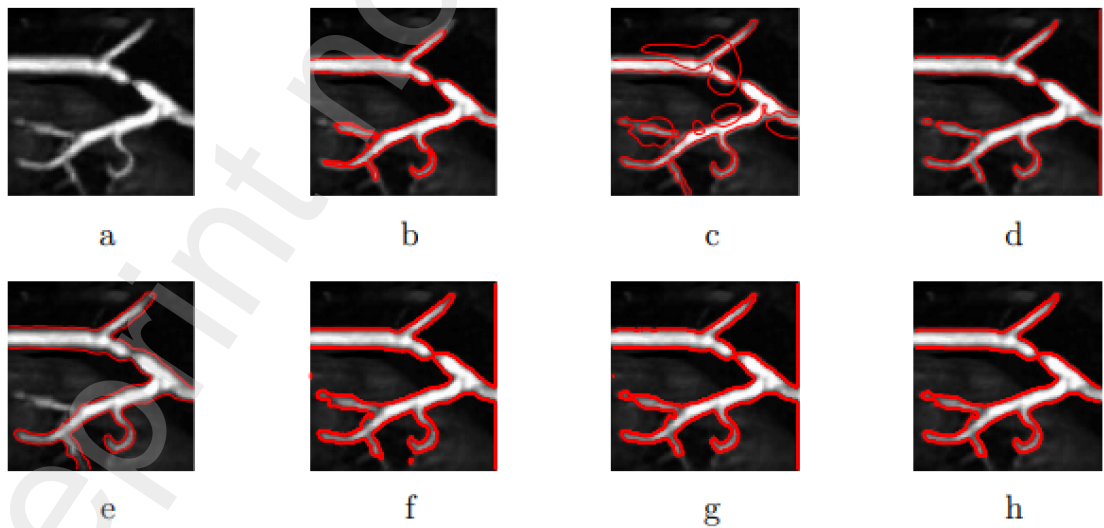

Fig. 10: The comparison between CV, LBF, SPGCS, LGDF, CCS, NAT and the proposed method on kidney vessel.
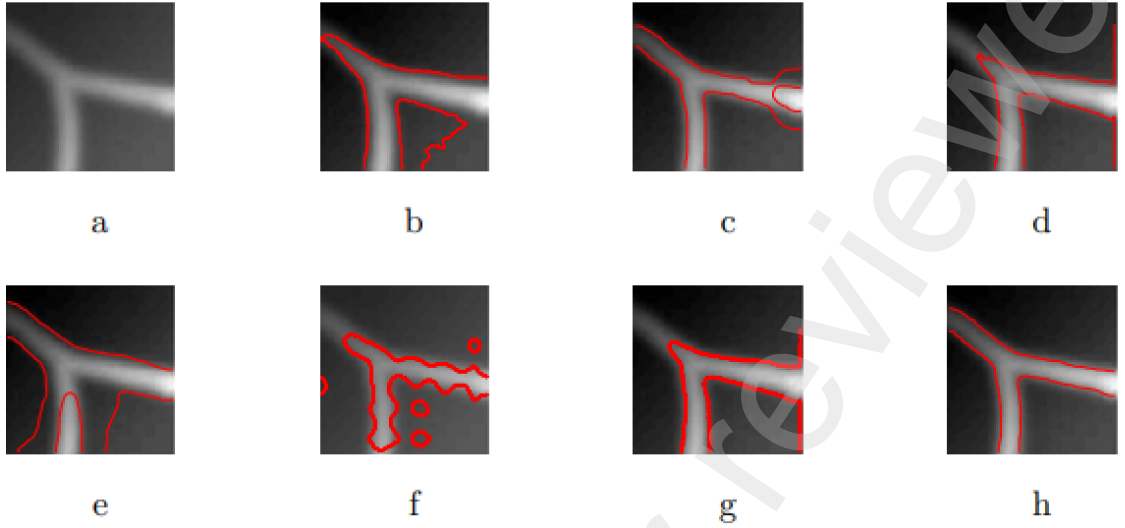
16

Fig. 11: The comparison between CV, LBF, SPGCS, LGDF, CCS, NAT and the proposed method on part of vessel.
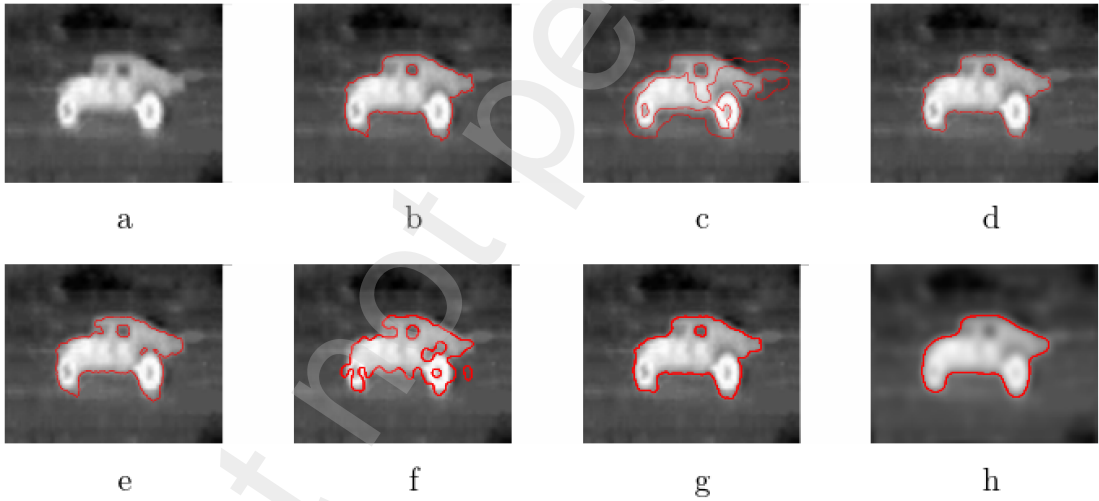

Fig. 12: The comparison between CV, LBF, SPGCS, LGDF, CCS, NAT and the proposed method on the military infrared image of car.

Algorithm	Js	F1	Recall	Precision	SA	κ
CV	0.9021	0.9105	0.9347	0.9141	0.9239	0.9331
LBF	0.5390	0.5647	0.4859	0.5111	0.5229	0.5759
SPGCS	0.9096	0.9119	0.9243	0.8923	0.9278	0.9049
LGDF	0.6804	0.6909	0.7211	0.7810	0.7314	0.7177
CCS	0.9110	0.9520	0.9889	0.9241	0.9800	0.9505
NAT	0.9089	0.9436	0.9873	0.9220	0.9749	0.9500
OUR	0.9175	0.9570	0.9896	0.9264	0.9888	0.9506

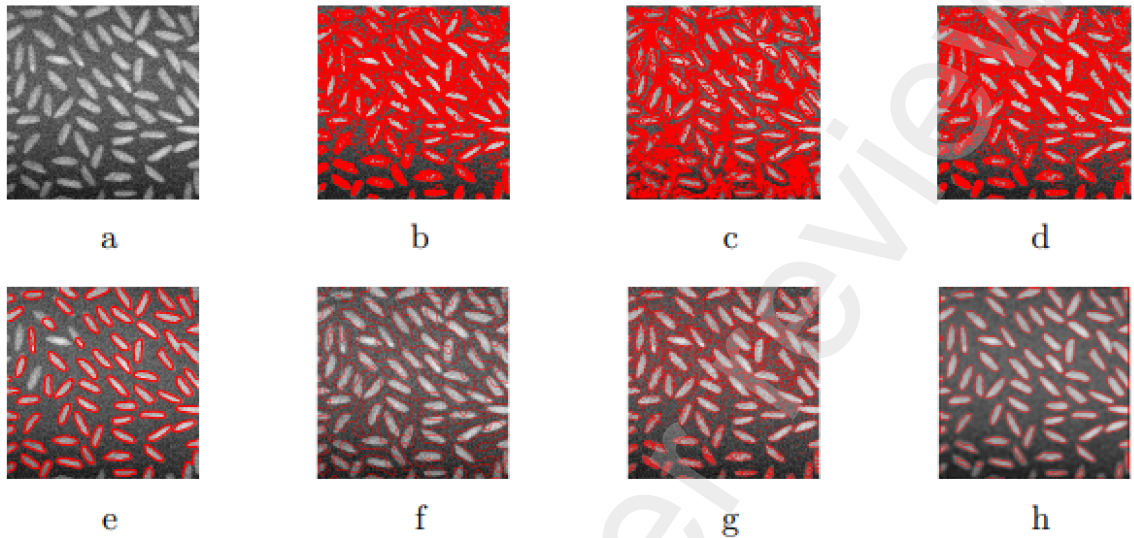Table 5: Six indecators of the segmentation results shown in Figure 16.

17

Fig. 13: The comparison between CV, LBF, SPGCS, LGDF, CCS, NAT and the proposed method on rice with noise.
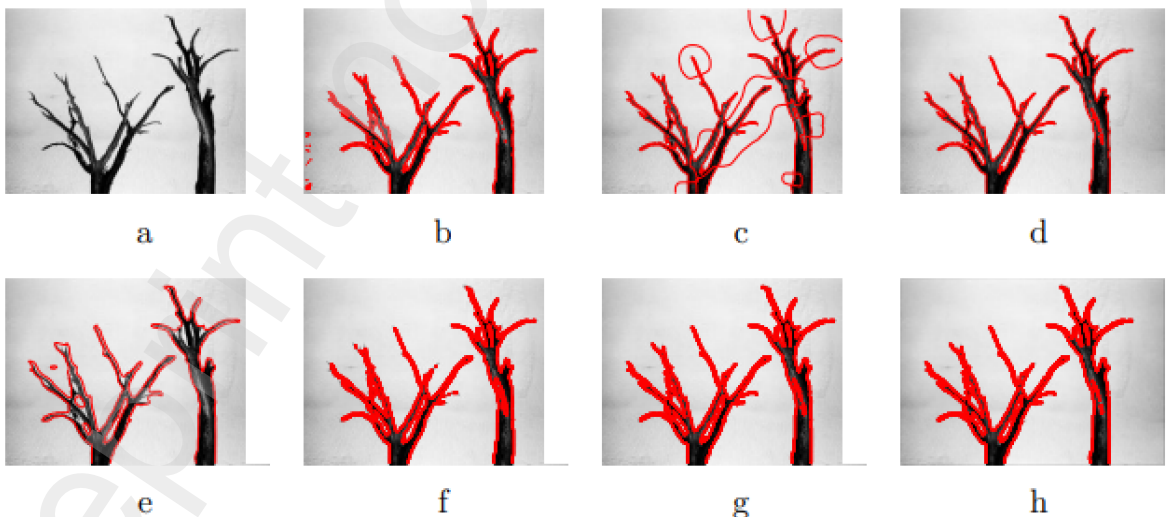

Fig. 14: The comparison between CV, LBF, SPGCS, LGDF, CCS, NAT and the proposed method on natural image of Tree.
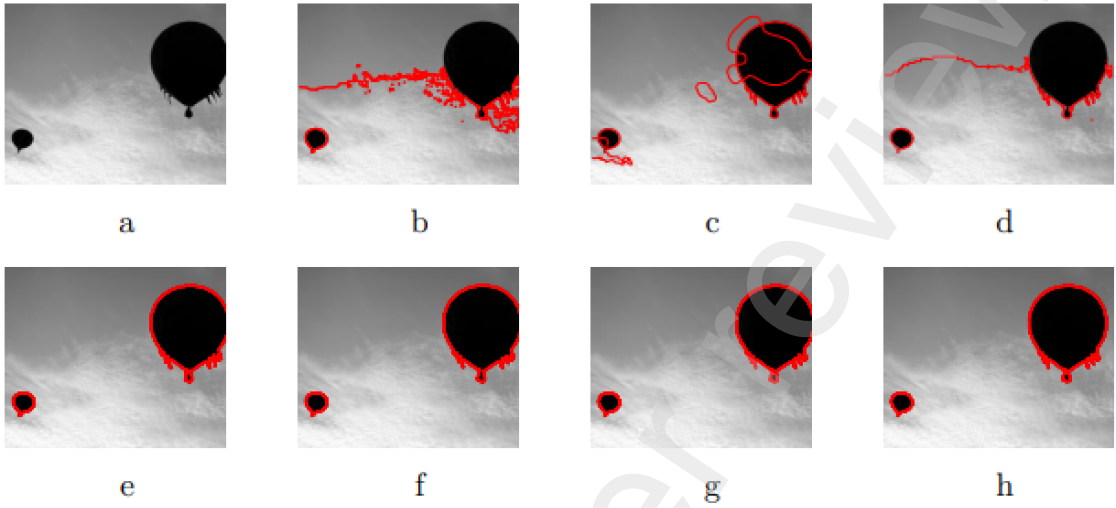
Fig. 15: The comparison between CV, LBF, SPGCS, LGDF, CCS, NAT and the proposed method on natural image of Balloon.
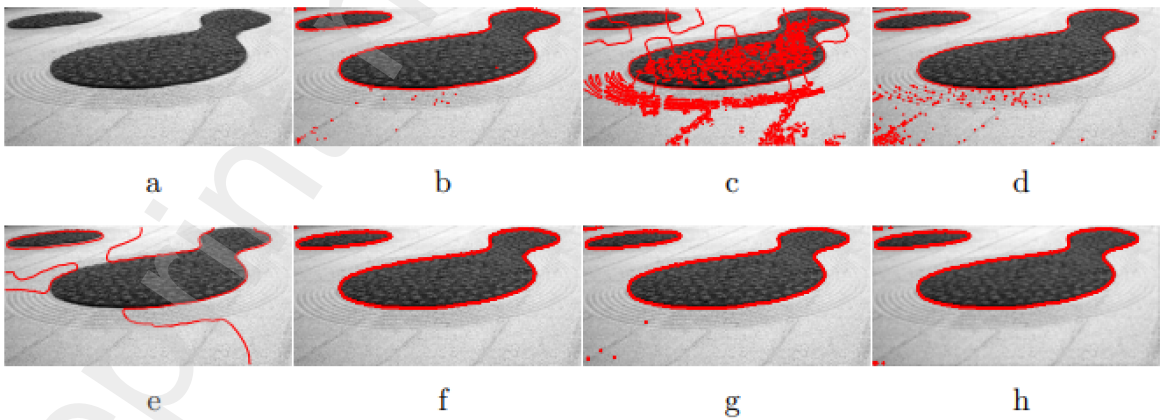

Fig. 16: The comparison between CV, LBF, SPGCS, LGDF, CCS, NAT and the proposed method on natural image of Partorre.
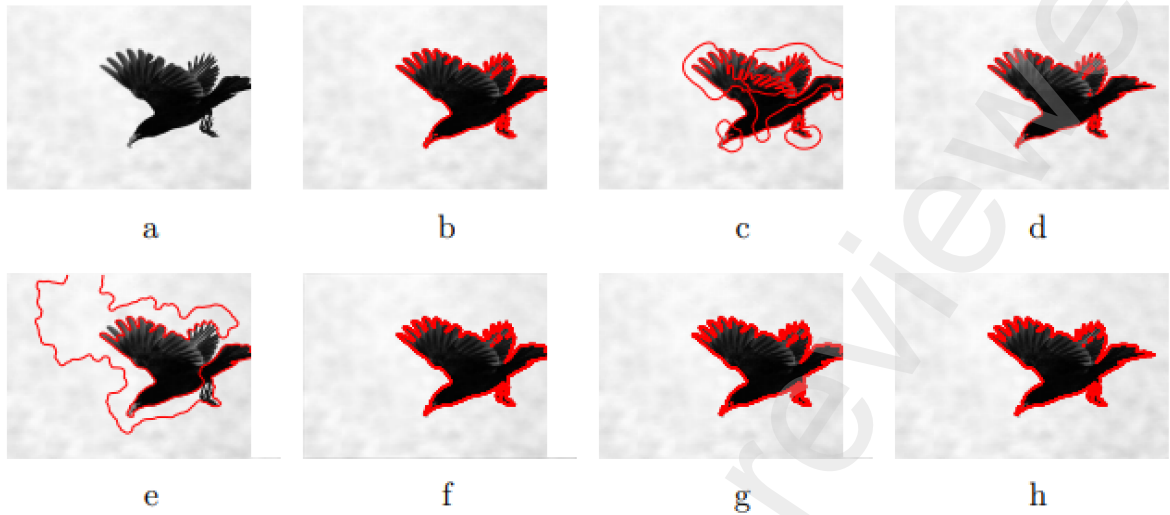
19

Fig. 17: The comparison between CV, LBF, SPGCS, LGDF, CCS, NAT and the proposed method on natural image of Eagle.

We also use Matlab codes to create the different blur operators: "fspecial('motion', 20, 45)", "fspecial('Gaussian', [15,15], 15)" and "fspecial('average',20)". The parameters of the operators are bigger than they set in algorithms [24] and [31]. The parameters of the algorithms are choosed the same values as: $\lambda = 100$ and $\eta = 1$. The segmentation results are shown in Figure 7-9. Our method has an improved ability to deal with the images with different blur.

4.3.2. Segmentation Images with weak boundary and low contrast

In this section, we apply the proposed method and the compared methods on the same images with weak boundary and low contrast. The compared methods are the state-of-the-art methods: CV[20], LBF [44], SPGCS [45], LGDF [46], CCS [24] and NAT [31]. As can be seen in Figure 10-13, Figure 10(a) is a magnetic resonance image of kidney blood vessels, Figure 11(a) is a biomedical image of part of blood vessel, Figure 12(a) is a military infrared image of a car. The boundaries of the objects are blurry and vague. Figure 13(a) is a classical image in image processing. It is an image of rice with noise. We can see from figure 10, only the CCS, NAT and our method can segment the right objects. When the paprameters are set the same and the thresholds are calculated automaticly. Only our method can achieve the desirable segmentation result. The segmentation results of other three images are exhibited in Figure 10-13. We can find that the proposed method delineates the boundaries of objects accurately.

4.3.3. Segmentation Natural Images

To futher demonstrate the superiority of our method, we perform experiments on natural images with ground truth. We also use the values of indicators to demonstrate the effectiveness of our method. The parameters are choosen suitable and fixed for these experimental images. The results are shown in Figure 14-17. The LBF and LGDF proved too much undesired scattered structures in the results. All the values of index are

20

presented in Table 2-5. It can be seen that our proprsed method provides the highest values compared to other approaches. Thus, our method is more reliable and stable for different natural images.

5. Conclusion

In this article, we develop a tensor voting based fractional-order image segmentation model. We introduce an effective global regularization term combined the structure tensor and fractional gradient which can smooth the details and preserve the characteristic structures of images. Our method inherits the merits of two-stage strategy which can improve the efficiency and performance during the restoration stage and segmentation stage. The minimization problem is solved by an ADI scheme which can split 2D problem into several uncondintionally stable 1D problem. Our method is low computational cost one which can be considered as the accelerated algorithm of other numerical schemes. Numerical experimental results on the synthetic, medical and natural images domonstrate the proposed method outpeforms several current advanced segmentation methods.

References

[1] Xie W, Liu D, Yang M, et al. SegCloud: A novel cloud image segmentation model using a deep convolutional neural network for ground-based all-sky-view camera observation[J]. Atmospheric Measurement Techniques, 2020, 13(4): 1953-1961.

[2] Rushing J A, Ranganath H, Hinke T H, et al. Image segmentation using association rule features[J]. IEEE Transactions on Image Processing, 2002, 11(5): 558-567.

[3] Li X, Yu L, Chen H, et al. Transformation-consistent self-ensembling model for semisupervised medical image segmentation[J]. IEEE Transactions on Neural Networks and Learning Systems, 2020, 32(2): 523-534.

[4] Eelbode T, Bertels J, Berman M, et al. Optimization for medical image segmentation: theory and practice when evaluating with dice score or jaccard index[J]. IEEE Transactions on Medical Imaging, 2020, 39(11): 3679-3690.

[5] Cholakkal H, Sun G, Khan F S, et al. Object counting and instance segmentation with image-level supervision[C]//Proceedings of the IEEE/CVF Conference on Computer Vision and Pattern Recognition. 2019: 12397-12405.

[6] Jiao X, Chen Y, Dong R. An unsupervised image segmentation method combining graph clustering and high-level feature representation[J]. Neurocomputing, 2020, 409: 83-92.

[7] N. Badshah, K. Chen, H. Ali, et al. Coefficient of variation based image selective segmentation model using active contours[J]. East Asian Journal on Applied Mathematics, 2(02)(2012), 150-169.

[8] J. Bramble, J. Pasciak, A. Vassilev, Analysis of the inexact Uzawa algorithm for saddle point problems[J]. SIAM Journal on Numerical Analysis, 34(3)(1997), 1072-1092.

[9] V. Caselles, R. Kimmel, G. Sapiro, Geodesic active contours[J]. Int. J. Comput. Vision 22 (1997), 61-79.

[10] D. Cremers, M. Rousson, R. Deriche, A review of statistical approaches to level set segmentation: integrating color, texture, motion and shape[J]. Int. J.Comput. Vision 72 (2007), pp. 195-215.

[11] D. Gupta, R. Anand. A hybrid edge-based segmentation approach for ultrasound medical images[J]. Biomedical Signal Processing and Control, 31(2017), 116-126.

[12] Chen D, Spencer J, Mirebeau J M, et al. A generalized asymmetric dual-front model for active contours and image segmentation[J]. IEEE Transactions on Image Processing, 2021, 30: 5056-5071.

[13] Zhang J, Chen K, Gould D A. A fast algorithm for automatic segmentation and extraction of a single object by active surfaces[J]. International Journal of Computer Mathematics, 2015, 92(6): 1251-1274.

[14] Wu C, Tai X C. Augmented Lagrangian method, dual methods, and split Bregman iteration for ROF, vectorial TV, and high order models[J]. SIAM Journal on Imaging Sciences, 2010, 3(3): 300-339.

[15] Zhang D, Tai X, Lui L M. Topology-and convexity-preserving image segmentation based on image registration[J]. Applied Mathematical Modelling, 2021, 100: 218-239.

[16] D. Mumford, J. Shah, Optimal approximation by piecewise smooth functions and associated variational problems[J]. Commun. Pure Appl. Math. 42 (1989), 577-685.

[17] Jauhiainen J, Seppänen A, Valkonen T. Mumford?Shah regularization in electrical impedance tomography with complete electrode model[J]. Inverse Problems, 2022, 38(6): 065004.

[18] Klann E, Ramlau R, Ring W. A Mumford-Shah level-set approach for the inversion and segmentation of SPECT/CT data[J]. Inverse Problems and Imaging, 2011, 5(1): 137.

[19] Ben-Ari R, Sochen N. Stereo matching with Mumford-Shah regularization and occlusion handling[J]. IEEE Transactions on Pattern Analysis and Machine Intelligence, 2010, 32(11): 2071-2084.

[20] T. Chan, L. Vese, Active contours without edges[J]. IEEE Trans. Image Process. 10 (2001), 266-277.

[21] Spencer J, Chen K. A convex and selective variational model for image segmentation[J]. Communications in Mathematical Sciences, 2015, 13(6): 1453-1472.

[22] Zhang J, Chen K, Yu B. A 3D multi-grid algorithm for the Chan-Vese model of variational image segmentation[J]. International Journal of Computer Mathematics, 2012, 89(2): 160-189.

[23] L. Vese, T. A multiphase level set framework for image segmentation using the Mumford and Shah model[J]. Int. J. Comput. Vision. 50 (2002), 271-293.

[24] Cai X, Chan R, Zeng T. A two-stage image segmentation method using a convex variant of the Mumford–Shah model and thresholding[J]. SIAM Journal on Imaging Sciences, 2013, 6(1): 368-390.

22

[25] Chan R, Yang H, Zeng T. A two-stage image segmentation method for blurry images with poisson or multiplicative gamma noise[J]. SIAM Journal on Imaging Sciences, 2014, 7(1): 98-127.

[26] Yu H, Jiao L, Liu F. CRIM-FCHO: SAR image two-stage segmentation with multi-feature ensemble[J]. IEEE Transactions on Geoscience and Remote Sensing[J]. 2015, 54(4): 2400-2423.

[27] Song J, Jiao W, Lankowicz K, et al. A two-stage adaptive thresholding segmentation for noisy low-contrast images[J]. Ecological informatics[J]. 2022, 69: 101632.

[28] Chen X, Zhou W. Smoothing nonlinear conjugate gradient method for image restoration using nonsmooth nonconvex minimization[J]. SIAM Journal on Imaging Sciences, 2010, 3(4): 765-790.

[29] Hintermüller M, Wu T. Nonconvex TV^q-models in image restoration: Analysis and a trust-region regularization–based superlinearly convergent solver[J]. SIAM Journal on Imaging Sciences, 2013, 6(3): 1385-1415.

[30] Yao Q, Kwok J T, Zhong W. Fast low-rank matrix learning with nonconvex regularization[C] 2015 IEEE International conference on data mining. IEEE, 2015: 539-548.

[31] Wu T, Shao J, Gu X, et al. Two-stage image segmentation based on nonconvex $l_2?l_p$ approximation and thresholding[J]. Applied Mathematics and Computation, 2021, 403: 126168.

[32] Pang Z F, Zhang H L, Luo S, et al. Image denoising based on the adaptive weighted TVp regularization[J]. Signal Processing, 2020, 167: 107325.

[33] Wu T, Gu X, Wang Y, et al. Adaptive total variation based image segmentation with semi-proximal alternating minimization[J]. Signal Processing, 2021, 183: 108017.

[34] F. Demengel, G, Demengel, Functional Spaces for the Theory of Elliptic Partial Differential Equations[M]. Springer, 2011: 219-224

[35] Han H, A variational model with fractional-order regularization term arising in registration of diffusion tensor image[J]. Inverse Problems and Imaging, 12(6) (2018) 1263-1291.

[36] Han H, Wang Z, An alternating direction implicit scheme of a fractional-order diffusion tensor image registration model[J]. Applied Mathematics and Computation, 356(2019) 105-118.

[37] Zhang J, Chen K. A total fractional-order variation model for image restoration with nonhomogeneous boundary conditions and its numerical solution[J]. SIAM Journal on Imaging Sciences, 2015, 8(4): 2487-2518.

[38] Han H. A tensor voting based fractional-order image denoising model and its numerical algorithm[J]. Applied numerical mathematics, 2019, 145: 133-144.

[39] Weickert J, Applications of Nonlinear Diffusion in Image Processing and Computer Vision[J]. Acta Math.univ.comenian,1 (2000) 33-50.

[40] Yang J, Guo Z, Zhang D, et al. An anisotropic diffusion system with nonlinear time-delay structure tensor for image enhancement and segmentation[J]. Computers and Mathematics with Applications, 2022, 107: 29-44.

[41] Estellers V, Soatto S, Bresson X. Adaptive regularization with the structure tensor[J]. IEEE Transactions on Image Processing, 2015, 24(6): 1777-1790.

[42] Li D, Zhang C, Ran M. A linear finite difference scheme for generalized time fractional Burgers equation[J]. Applied Mathematical Modelling, 2016, 40(11-12): 6069-6081.

23

[43] Y. Zhang, Z. Sun, Error analysis of a compact ADI scheme for the 2D fractional subdiffusion equation[J]. Journal of Scientific Computing, 59(1)(2014) 104-128.

[44] X. Wang, D. Huang, H. Xu, An efficient local Chan-Vese model for image segmentation[J]. Pattern Recognition.43(3)(2010), 603-618.

[45] Goldstein T, Bresson X, Osher S. Geometric applications of the split Bregman method: segmentation and surface reconstruction[J]. Journal of scientific computing, 2010, 45: 272-293.

[46] L. Wang, C. Li, Q. Sun, D. Xia, C.Y. Kao, Active contours driven by local and global intensity fitting energy with application to brain MR images segmentation[J]. Comput. Med. Imag. Graph. 33 (2009), 520-531.

24